ENGINEERING

Addressing transconductance-bandwidth trade-off by three-dimensional electrolyte-surrounded organic electrochemical transistors

Yongwoo Lee[1,2]†, Seong Jun Park[3]†, Jimin Kwon[2]*, Kang-Il Song[4]*, Sungjune Jung[1,3]*

The performance of organic electrochemical transistors (OECTs) is fundamentally constrained by a trade-off between transconductance and temporal response. While increasing channel thickness enhances its capacitance and thereby amplifies transconductance, it simultaneously impedes ion transport kinetics, leading to slower switching speeds. Here, we present a three-dimensional electrolyte-surrounded OECT architecture that redefines ion transport dynamics by enabling multidirectional ion doping to the channel for efficient and rapid switching. Our proposed approach achieves a remarkable enhancement in the operational bandwidth of OECTs, reaching 26 kHz while preserving their high transconductance, notably using a commercially available conductive polymer, poly(3,4-ethylenedioxythiophene):poly(styrenesulfonate). This is enabled by micro/nanostructured channel design that enhances ion accessibility and minimizes parasitic effects. This advancement allows for continuous, wide-frequency neural signal recording from peripheral nerves. This work offers a robust strategy for achieving both high transconductance and fast switching in OECTs, establishing a foundation for the development of next-generation, high-speed bioelectronic interfaces.

INTRODUCTION

Organic bioelectronics has emerged as an innovative and promising field, exploring and leveraging the distinctive properties of organic semiconductors at the interface with cells, tissues, and biological systems (*1*–*4*). Central to the emerging organic bioelectronics paradigm, organic electrochemical transistors (OECTs) are heralded for their unique advantages over conventional transistor technologies, particularly in the fields of biosensor (*5*–*9*), such as electrophysiology (*10*–*13*) and neuromorphic circuit (*14*–*18*). Their notable features include operation at subvolt voltages with high transconductance, a simplified device structure without a gate dielectric, mixed ionic and electronic conduction, and compatibility with aqueous electrolytes like biological media. Additionally, their fabrication on the biocompatible, flexible substrate via additive printing processes makes them ideal for integrating electronic and biological systems (*19*, *20*). These characteristics highlight OECTs as a versatile tool for advancing bioelectronic interfaces.

A crucial requirement for bioelectronic devices is to achieve high transconductance g_m (defined as the derivative of the drain current, I_D, with respect to the gate voltage, V_G; i.e., $\partial I_D/\partial V_G$), which must remain consistent across the broad frequency spectrum associated with the human body's electrical activities. For example, while electroencephalography captures signals below 40 Hz, recording single-neuron action potential requires devices that can accurately measure much higher frequencies, typically in the range of 1 to 5 kHz (*21*–*27*). Further enhancing the bandwidth of OECTs will improve their compatibility with diverse bioelectronic platforms, facilitating more accurate, real-time detection and processing of high-frequency physiological signals. OECT devices operate by volumetric ion penetration into the channel, offering high transconductance through bulk doping. However, this volumetric operation imposes a kinetic bottleneck, where increased channel thickness enhances gain at the expense of response speed. In contrast to field-effect transistors, which exhibit lower transconductance (typically, in the microsiemens range) but can operate at higher frequencies (*28*–*30*), OECTs achieve high transconductance in the range of millisiemens, with their frequency response tapering off above a few hundred hertz (*31*). This fundamental transconductance-bandwidth trade-off limits their application in high-speed bioelectronics that require high-frequency operation.

Various strategies have been used to enhance the bandwidth of OECTs. A straightforward method is to reduce the channel thickness or decrease the concentration of secondary polar dopants, which can accelerate response times (*32*–*34*). While incorporating additives such as crown ethers into organic mixed ionic-electronic conductors (OMIECs) has led to improved bandwidth and transconductance (*35*), the biocompatibility and long-term stability of such modifications still require further validation. Applying a step input voltage has also proven effective in achieving millisecond-scale response times by producing a square step in the drain current without exponential relaxation (*36*). Furthermore, the development of vertical channel OECTs, which decrease channel lengths to submicron scales and increase device density through stacked integration in the *z* direction, represents a notable advancement (*37*–*40*). Another approach is to expand the interface area between the electrolyte and the channel, using nanomesh (*41*, *42*) or nanofiber (*43*, *44*) architectures to promote efficient ion injection, thereby shortening the ion travel distance for doping and dedoping processes. However, these approaches generally result in a considerable reduction in volumetric capacitance, leading to decreased amplification, exhibiting uneven conductivity across the channel, or necessitating maintaining the drain voltage within a

[1]Department of Convergence IT Engineering, Pohang University of Science and Technology (POSTECH), 77 Cheongam-Ro, Nam-Gu, Pohang 37673, Gyeongbuk, Republic of Korea. [2]Department of Electrical Engineering, Ulsan National Institute of Science and Technology (UNIST), 50 UNIST-gil, Ulju-gun, Ulsan 44919, Republic of Korea. [3]Department of Materials Science and Engineering, Pohang University of Science and Technology (POSTECH), 77 Cheongam-Ro, Nam-Gu, Pohang 37673 Republic of Korea. [4]Division of Smart Healthcare, Pukyong National University, Busan 48513, Republic of Korea.
*Corresponding author. Email: jmkwon@unist.ac.kr (J.K.); kangil.song@pknu.ac.kr (K.-I.S.); sjjung@postech.ac.kr (S.J.)
†These authors contributed equally to this work.

narrow operational range ($V_D \ll V_T$-V_G). Recent progress in internal ion-gated OECTs has demonstrated microsecond-scale response times by embedding mobile ions directly within the channel and incorporating ion membranes on top (*45*–*47*). While this configuration enables rapid and spatially confined doping/dedoping dynamics, it requires additional fabrication steps and specialized materials that may limit integration with scalable or biocompatible platforms. These constraints demand a critical need for OECT designs that can address the trade-off between transconductance and bandwidth without introducing architectural complexity, particularly for bioelectronic systems that demand both high signal amplification and fast response at frequencies exceeding the kHz range.

Here, we introduce the three-dimensional electrolyte-surrounded (3D ES) OECTs featuring micro/nanostructured channel architecture that can effectively mitigate the intrinsic transconductance-bandwidth trade-off inherent to conventional planar OECT. This ES OECT architecture markedly enhances the channel's surface-to-volume ratio, substantially improving ionic penetration efficiency without compromising transconductance. To evaluate the impact of this architecture, we systematically fabricated and characterized ES OECTs with varying micro- and nanostructured channel patterns. We first performed static electrical measurements to confirm that the intrinsic electronic properties of the active channel remain unaffected by the structural modifications, ensuring stable transconductance and uniform device performance. We then conducted dynamic response analyses, including transient and frequency-domain measurements, to assess the enhancement in switching speed and operational bandwidth. By comparing ES OECTs with conventional planar devices, we demonstrate that the modified architecture effectively reduces ionic transport delays, leading to a notable improvement in response time. Moreover, we validate the practical utility of ES OECTs through their integration into an active neural probe, where they enable high-fidelity recording of bioelectrical signals across a broad frequency range. These findings establish the ES architecture as a scalable and high-performance solution for bioelectronic applications requiring both high sensitivity and rapid signal processing.

RESULTS

Mitigating transconductance-bandwidth trade-off by 3D ES OECTs

We have developed an ES architecture for OECTs that substantially enhances the operational speed by reducing the effective ionic path required for channel doping and dedoping dynamics. Incorporating micro- or nanostructures into the channel architecture allows ions from the electrolytes to simultaneously penetrate from all directions around the entire channel, notably reducing ionic diffusion pathways and greatly expanding the channel-electrolyte interface area. As illustrated in Fig. 1A, in planar OECTs, a gate voltage drives an ionic charge carrier from the electrolyte into the OMIEC channel, thereby modulating its conductivity. In this architecture, as channel volume increases to achieve higher transconductance, its operating speed inevitably slows down due to charge carriers moving unidirectionally along a prolonged ionic path, while the electrolyte-channel interface remains constant despite the volume changes. In contrast, the 3D ES structure enables ions to access the micro- or nanostructured channel in a manner that allows the surface area of the channel to increase proportionally with volume change. Unlike planar OECTs, which are limited by a trade-off between transconductance and bandwidth as

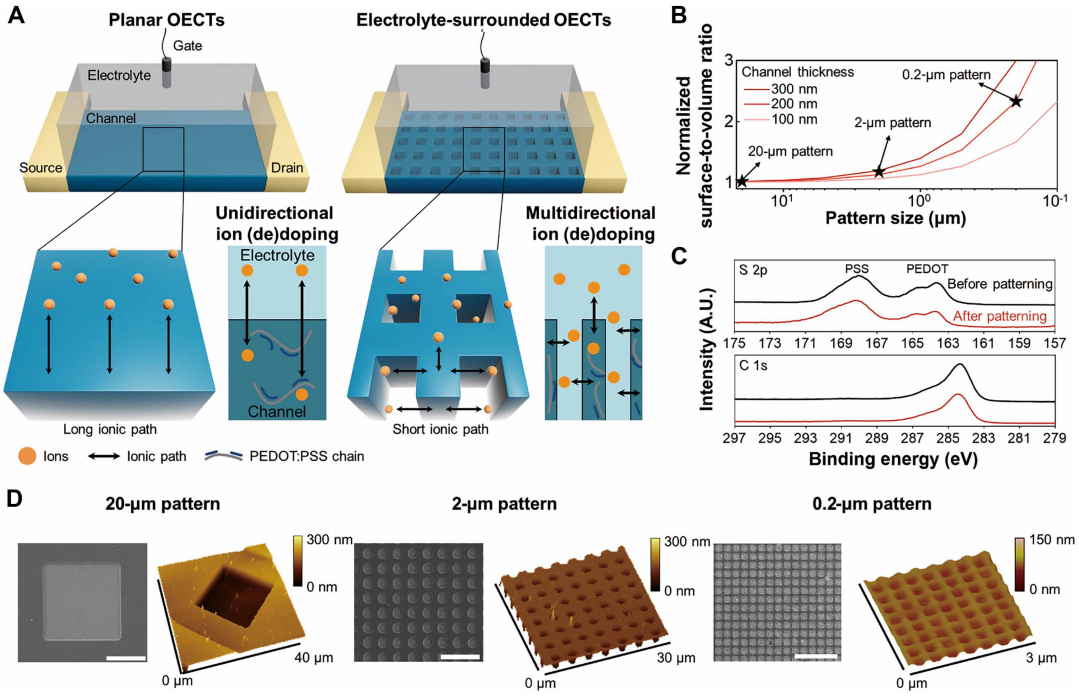

Fig. 1. 3D ES OECTs. (**A**) Schematic of a planar OECTs structure with ion movement between the electrolyte and cuboid channel, and an ES OECTs structure with effective ion movement between the electrolyte and concave-convex channel. (**B**) Theoretical surface-to-volume ratio with various channel thicknesses. Black stars indicate our experimental values of ES OECTs with channel pattern sizes (20, 2, and 0.2 μm). (**C**) Comparison of the x-ray photoelectron spectroscopy spectra of S 2p and C 1s before and after channel structure patterning. A.U., arbitrary units. (**D**) Scanning electron microscopy (SEM) and atomic force microscopy (AFM) images for each channel pattern size (20, 2, and 0.2 μm). The scale bars represent 10 μm (left, middle) and 2 μm (right).

channel volume increases, the ES OECTs maintain efficient all-around ionic diffusion regardless of channel volume. This unique feature enables simultaneous achievement of high transconductance and wide operational bandwidth. Theoretical calculations suggest that the surface-to-volume ratio can be meaningfully enhanced with smaller channel pattern dimensions and thicker channels (Fig. 1B and fig. S1). Consequently, the shortened ionic paths and increased surface-to-volume ratio of the channel structure not only facilitate efficient ion injection into the channel, thereby improving the transient response of ES OECTs but also enable effective amplification of biological signals across a broad frequency spectrum, including high-frequency neural signals (fig. S2). Micro- and nanostructured poly(3,4-ethylenedioxythiophene):poly(styrenesulfonate) (PEDOT:PSS) channel created using maskless laser and electron (e)–beam lithography techniques (fig. S3). X-ray photoelectron spectroscopy was used to identify that channel structure patterning barely affects the elemental composition of the OMIEC channel (Fig. 1C). The conformational characteristics of the ES OECT geometry for each pattern size (20, 2, and 0.2 μm) were characterized using scanning electron microscopy (SEM) and atomic force microscopy (AFM), respectively (Fig. 1D).

Static electrical characterization of 3D ES OECTs

To investigate the impact of micro/nanostructures on the static electrical characteristics, we fabricated OECT devices with channel patterns sized at 0.2, 2, and 20 μm. The channel width/length (W/L) for 0.2 μm pattern was designed as 50/25 μm and 400/40 μm for 2 and 20 μm patterns, respectively. The maximum transconductance ($g_{m,max}$) normalized with the channel dimension remained consistent across these different pattern sizes, which is in good agreement with values reported for PEDOT:PSS-based planar channel OECTs (Fig. 2A) (*33*, *48*). This consistency confirms that the intrinsic properties of the channel remained unchanged during the patterning process. The ES

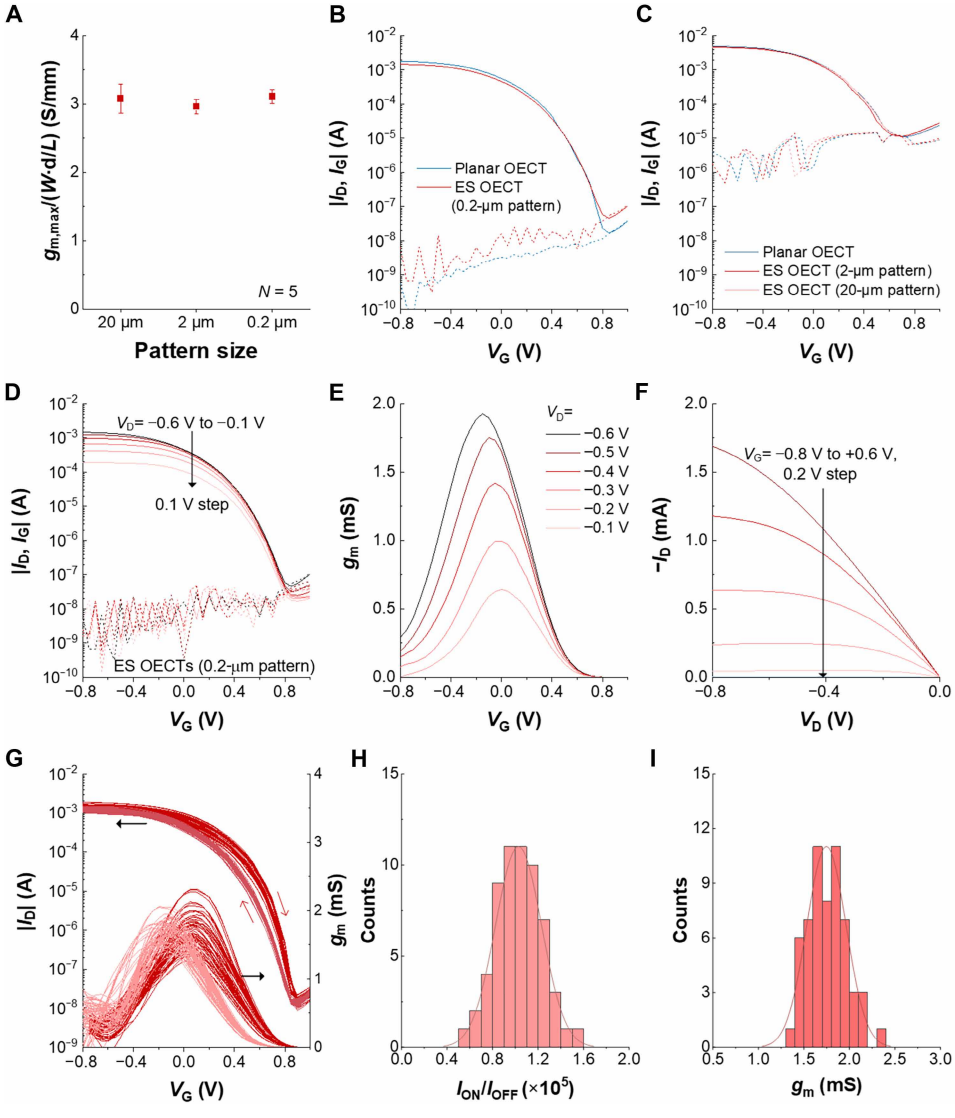

Fig. 2. Electrical characteristics of 3D ES OECTs. (**A**) Comparison of the maximum transconductance normalized by channel for different pattern sizes (0.2, 2, and 20 μm). (**B**) Transfer characteristics of planar and ES OECTs (0.2-μm pattern) with W/L = 50/25 μm. (**C**) Transfer characteristics of planar and ES OECTs (2 μm, 20-μm pattern) with W/L = 400/40 μm. (**D**) Transfer characteristics with various drain voltages, (**E**) transconductance, (**F**) output characteristics of ES OECTs (0.2-μm pattern) with W/L = 50/25 μm. (**G**) Statistical dual-sweep transfer characteristics, (**H**) histogram of the on/off current, and (**I**) transconductance for 60 ES OECTs (0.2-μm pattern) with W/L = 50/25 μm.

OECTs with patterns of 0.2 and 20 μm demonstrated reliable transfer characteristics, showing negligible deviation from planar OECTs with equivalent channel volume (Fig. 2, B and C). We also assessed the drain bias dependency and gate leakage current to evaluate the robustness of the device architecture. The 0.2-μm structured ES OECTs exhibited negligible gate leakage across the entire operating gate voltage range and under various drain biases (Fig. 2D). The minimal variation in subthreshold slopes suggests stable operation and confirms that the 3D ES structure does not compromise electrostatic gate control over the channel. Transfer characteristics for the 2- and 20-μm patterned ES OECTs are detailed in fig. S4. Negligible hysteresis was observed from dual-sweep transfer characteristics measured with varying sweep delay times for a 0.2-μm OECT (fig. S5). Transconductance as a function of gate voltage for different drain voltages exhibited the typical nonmonotonic dependence observed in planar PEDOT:PSS film-based OECTs, with $g_{m,max}$ shifting to the left as the drain voltage increased (Fig. 2E) (*49*, *50*). Output characteristics of the ES OECTs with gate voltages ranging from −0.8 to +0.6 V (in 0.2-V steps) demonstrated clear pinch-off and saturation regions (Fig. 2F). To verify the uniformity of ES OECT fabrication, we produced 60 transistors with a 0.2-μm patterned channel. All devices exhibited consistent and reliable electrical characteristics without any nonfunctioning units observed (Fig. 2G). Histograms of the statistical variation in the on/off ratio of drain current and transconductance are presented in Fig. 2 (H and I), with each Gaussian fit yielding a mean on/off ratio of 1.03×10^5, g_m of 1.75 mS with a SD of 0.2×10^5 and 0.22 mS at $V_D = -0.6$ V, respectively. These consistent transconductances, stable transfer characteristics, negligible gate leakage, and uniform device performance across multiple fabrications highlight the robustness and scalability of the 3D ES architecture for high-performance OECT applications.

Dynamic electrical characterization of 3D ES OECTs

Following the confirmation of reliable and reproducible static characteristics of ES OECTs, we investigated the enhancement in dynamic performance enabled by the 3D ES architecture, specifically examining both transient and frequency responses. Drain current transient responses for OECTs with different pattern sizes were measured by applying repeated square waveform pulses to the gate electrode, from which turn-on (τ_{ON}) and turn-off (τ_{OFF}) time constants were extracted. The changes in τ_{ON} and τ_{OFF} normalized with nonpatterned planar OECTs show that the shortened ionic paths within the OMIEC enable markedly improved volumetric doping/dedoping dynamics. A comprehensive comparison among devices with varying pattern sizes and a planar counterpart is presented in Fig. 3A, where ES OECTs consistently exhibited faster responses than their planar equivalents with matched channel volumes and transconductance. Detailed statistical data of the electrical performance for each device type are summarized in table S1. Notably, as the structure dimensions scaled from the microscale to the nanoscale, the improvement in response time was increasingly pronounced. For example, a representative transient response from a 0.2-μm patterned device demonstrated a marked reduction of τ_{ON} from 68.8 to 21.7 μs and τ_{OFF} from 35.4 to 19.5 μs, compared to the planar OECT (Fig. 3B); the transient responses for the 2- and 20-μm patterned devices are presented in fig. S6. The findings indicate that the shortened ionic pathways in the 3D ES architecture enhance the efficiency of ion redistribution under gate voltage modulation. This is supported by electrochemical impedance spectroscopy (EIS) measurements and equivalent circuit modeling (fig. S7), which reveal comparable channel capacitance between ES and planar OECTs but substantially reduced ionic resistance in the ES channel, most notably in the 0.2-μm patterned device. Furthermore, the observed rightward phase shift in the Bode plot provides additional evidence of more efficient ionic doping and dedoping dynamics in ES devices. The ES OECTs achieved a notably higher cutoff frequency (f_c = 7.9 kHz), defined as a −3-dB roll-off point of the measured g_m, compared to 2.3 kHz for planar devices while maintaining a comparable transconductance (Fig. 3C). The agreement between the extracted time constants and the theoretical relationship $1/2\pi f_c \approx \tau_{ON}$ further validates the accuracy of our speed measurements. Figure S8 presents a comparative analysis of the frequency response characteristics before and after channel patterning, which modifies the channel volume through the etching process. While the patterned ES architecture yields a considerable enhancement in bandwidth, this comes at the cost of a moderate reduction in transconductance, attributable to the reduced volumetric capacitance. However, this trade-off can be effectively mitigated by increasing the channel thickness. As a result, the overall transconductance–bandwidth product (g_mBP) of the ES OECTs substantially surpasses that of their planar counterparts, highlighting their potential for high-speed bioelectronic applications.

To assess the device stability under repetitive switching, we applied 150 square pulses with a 100-μs width to the gate over a 30-ms period. As shown in Fig. 3D, the device reliably exhibited consistent switching behavior with stable transient responses. Notably, we achieved the fastest response time among external ion-gated OECTs using common PEDOT:PSS formulations, such as ethylene glycol addition. Our 3D ES device, with a channel width and length of 20 and 10 μm, respectively, attained τ_{ON} of 4.1 μs and τ_{OFF} of 3.2 μs, representing ~2× to 3× improvement in response speed over planar counterparts (τ_{ON} of 13.6 μs and τ_{OFF} of 10.2 μs) while maintaining comparable transconductance (Fig. 3E). The corresponding f_c was determined to ~26 kHz, resulting in a record g_mBP of slightly above 10^4 Hz·mS, a crucial figure of merit calculated as the product of bandwidth and the transconductance (Fig. 3F). To provide deeper insight into performance trade-offs between different PEDOT:PSS-based OECT architectures, we plotted the operating cutoff frequency f_c against the maximum of transconductance $g_{m,max}$. As illustrated in Fig. 3G and summarized in table S2, our ES OECTs clearly outperformed previously reported PEDOT:PSS-based transistor architectures, including nanomesh, nanofiber, and vertical channel designs (*33*–*35*, *37*, *40*, *41*, *43*, *45*–*47*, *51*–*53*). The exceptional g_mBP achieved here indicates that further structural development and optimization, such as increasing the aspect ratio of the 3D ES pillar structures or using thicker channel films, could further enhance the surface-to-volume ratio at the electrolyte-channel interface and shorten ionic diffusion pathways, ultimately maximizing the achievable g_mBP.

In vivo demonstration of high-frequency neural signal recording

To validate practical applicability, 3D ES OECT-based active neural probes were implanted in rat sciatic nerves, and neural signal activities were recorded during mechanical stimuli on mechanoreceptors in the foot (Fig. 4A). The implanted OECT neural probe was conformally positioned to wrap around the sciatic nerve. Owing to the low modulus of nerves, the neural probe was provided with strategies to ensure biocompatibility and compressive stress relief. The ultrathin and flexible parylene substrate of OECT helps alleviate continuous compressive forces, preventing fascicle deformation (Fig. 4B). To compare the performance of both types of planar and ES OECTs

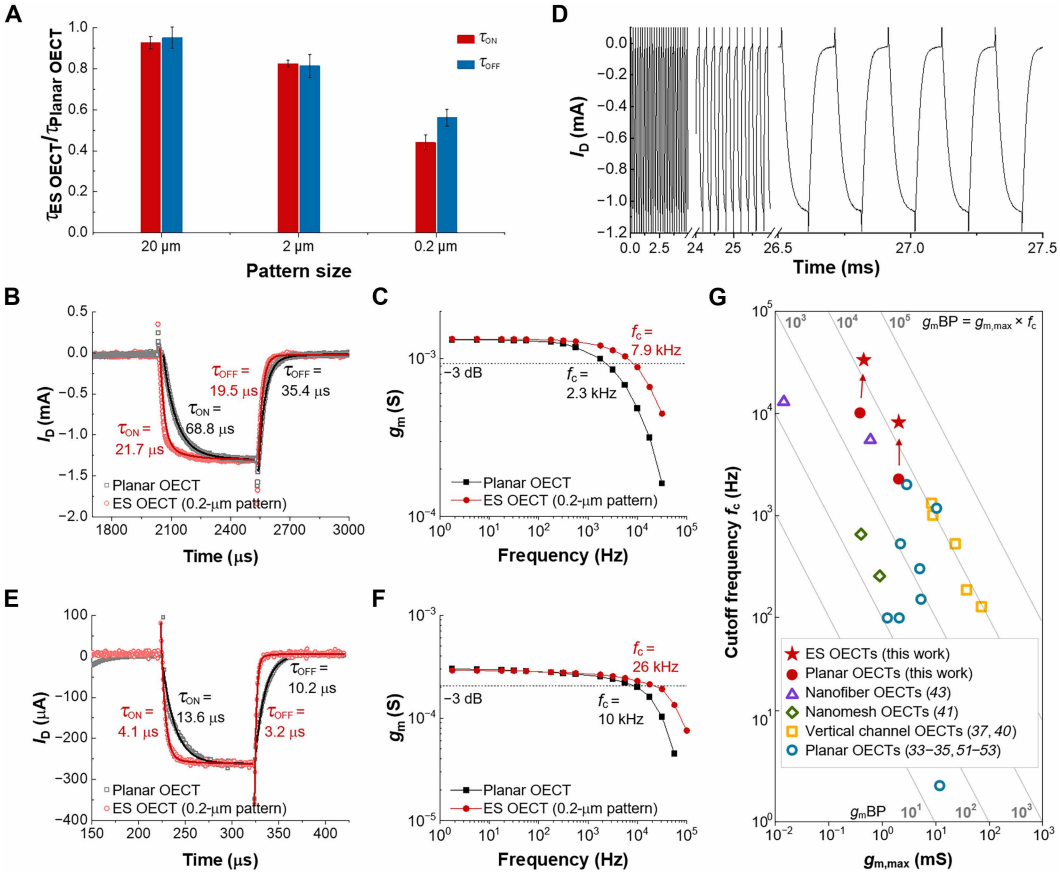

Fig. 3. Transient and frequency response of 3D ES OECTs. Comparison of the normalized (**A**) turn-on (τ_{ON}) and turn-off (τ_{OFF}) time constants extracted from transient measurement for different pattern sizes (0.2, 2, and 20 μm) relative to planar OECTs, under matched transconductance. $N = 5$. (**B**) Transient drain current response of planar and ES OECTs (0.2-μm pattern). A square pulse gate voltage of ±0.6 V was applied, and $V_D = -0.6$ V. The extracted time constant τ values were obtained by fitting the drain current response using the equation $y = y_0 + A_1 e^{-(x-x0)/\tau}$. Experimental data are shown as hollow symbols (red circles for ES and gray squares for planar), and fitting results are shown as solid lines (red for ES and black for planar). (**C**) g_m-frequency characteristics of planar and ES OECTs (0.2-μm pattern) with a cutoff frequency (f_c) guideline. (**D**) Cycling stability of ES OECTs (0.2-μm pattern). (**E**) Fastest temporal response of the drain current of ES OECTs ($W = 20$ μm and $L = 10$ μm) compared with planar OECT performance. (**F**) Corresponding frequency dependence of transconductance with a −3-dB line. (**G**) Comparison of $g_{m,max}$ and cutoff frequency f_c for ES OECTs (this work) and various PEDOT:PSS-based OECT architectures reported in literature. Gray diagonal lines represent constant transconductance–bandwidth product (g_mBP) contours. The ES OECTs shown in red stars correspond to devices with channel patterns of 0.2 μm. Corresponding planar OECTs with the same channel dimension are shown as red circles.

simultaneously, we placed the two types of OECT devices on the OECT neural probe in the longitudinal direction of neural signal transmission. The recorded signal is connected to an external circuit in the form of a common-source amplifier, which converts it to a voltage and then passes it to the data acquisition system.

For the planar OECTs, the amplification characteristics decrease rapidly beyond kHz, whereas ES OECTs can maintain relatively high amplification gains into the higher frequency regimes. The measured neural signals were changed with the neural state of the sciatic nerve of the rat in real time, and time-frequency analysis of neural activities recorded by our OECT neural probe was shown (Fig. 4C). The ES OECTs and planar OECT recorded neural signals simultaneously during the stimulus-present period and the stimulus-absent period. The recorded signals could be different because the active channel of each device is in different parts of the nerve. The evoked action potential observed in the ipsilateral nerve is a result of mechanical stimulation applied to the limb using a brush. The results of the time-frequency analysis indicated that, during the mechanical stimuli, a strong signal was detected between 500 Hz and 5 kHz. The signal-to-noise ratio (SNR) obtained from ES OECTs (SNR of 5.08) was superior to that of the signals obtained from planar OECTs (SNR of 3.95). SNR was defined as the ratio of the root mean voltage of the evoked neural signal to the root mean voltage of the remaining neural signals. The planar OECTs faced challenges in accurately detecting peripheral nerve signals within the frequency range. For ES OECTs, on the other hand, the cutoff frequency is shifted toward higher values, enabling the preservation of relatively high amplification characteristics throughout a broad range of frequencies. The results of these neural signal recordings directly demonstrate the effects of the 3D ES structure.

DISCUSSION

Biological systems rely extensively on ions for critical physiological functions, such as signal transduction, information storage, and maintaining cellular homeostasis, analogous to electrons in conventional electronic systems. OECTs, built upon OMIECs, uniquely facilitate the simultaneous conduction and processing of both electronic and ionic signals via an electron-ion charge compensation mechanism. This

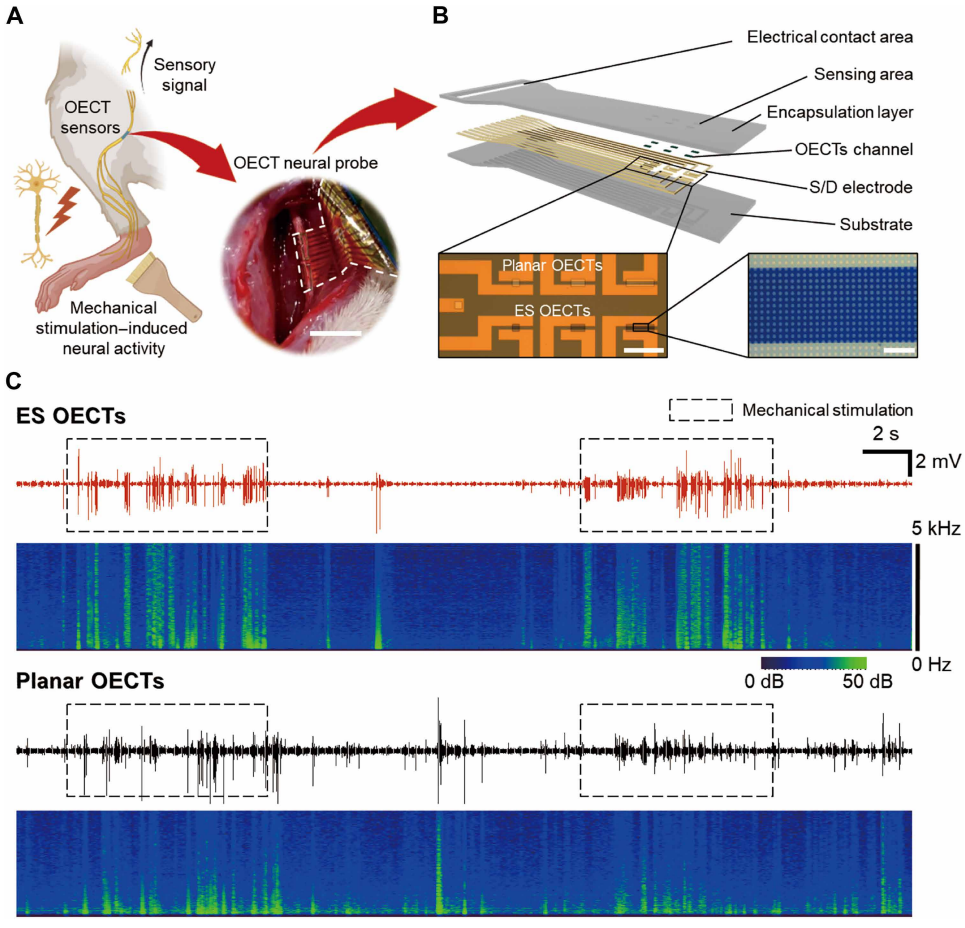

Fig. 4. Continuous peripheral neural signal monitoring by using 3D ES OECTs. (**A**) Schematic and photography of the OECTs neural probe with planar and ES, interfacing with a rat sciatic peripheral nerve. The scale bar represents 5 mm. (**B**) 3D schematic and microscopic images of the OECTs neural probe and channel details. S/D, source/drain. The inset shows the close-up ES channel pattern. The scale bars represent 500 μm (left) and 20 μm (right). (**C**) Synchronized sensory neural signals and spectrograms with and without mechanical stimulation in the OECTs channel (i.e., ES and planar). The presented data are 0.5 to 5 kHz band-pass filtered.

exceptional property enables their seamless integration into bioelectronic interfaces, effectively bridging electronic systems and biological environments (*20*, *54*–*56*). A key performance parameter of OECTs, transconductance, directly governs signal amplification but inherently faces a trade-off with the device's operational speed. Conventional planar OECTs experience slower ionic doping and dedoping kinetics as their channel volume increases, which is necessary to achieve higher transconductance. This limitation can be understood through an equivalent RC circuit model, in which device transient behavior is characterized by an exponential response defined by a time constant (τ), expressed as a product of the resistance of electrolyte (R_s) and channel capacitance (C_{ch}). Consequently, increasing channel volume to enhance higher device gain inevitably prolongs ionic diffusion paths, reducing operational bandwidth and thus limiting their application in high-frequency bioelectronic interfaces.

On the contrary, our proposed 3D ES architecture enables significant bandwidth enhancement without sacrificing transconductance performance. By introducing micro- and nanoscale structural features, the 3D ES configuration shortens ion diffusion distances, independent of channel volume, thereby substantially improving volumetric doping/dedoping dynamics. The increase in surface-to-volume ratio ensures efficient and rapid ion penetration and release, enhancing transient response without sacrificing transconductance. Notably, recent operando x-ray fluorescence studies of PEDOT:PSS have revealed that ion transport along polymer interfaces can be faster than bulk transport due to enhanced local ion density and shorter effective drift-diffusion lengths (*57*). Although our ES configuration differs structurally, the considerably increase in electrolyte-exposed surface area could facilitate similar interfacial effects, possibly contributing to the improved response characteristics observed. To further elucidate these interfacial contributions, future work involving in situ spectroscopy will be important for directly tracking the spatiotemporal dynamics of ion doping within complex 3D architectures. Crucially, this approach scales advantageously with increased channel volumes, a feature impossible to achieve in planar devices.

Our experimental results demonstrate markedly enhanced transient and frequency response characteristics, validated by a substantial increase in cutoff frequency as the channel pattern size is scaled down. Notably, the 3D ES OECTs achieved cutoff frequencies up to 26 kHz and an unprecedented g_mBP exceeding 10^4 Hz·mS, surpassing the performance of both planar and previously reported high-speed OECT architectures. These results highlight the effectiveness of the 3D ES design in mitigating the long-standing trade-off between transconductance-bandwidth in OECT. By enabling high-gain, high-speed operation

within a structurally simple and fabrication-compatible framework, this platform represents an important development for next-generation bioelectronic interfaces. Future work may further exploit structural parameters, such as pillar geometry and thicker channels, to push the performance envelope and broaden the scope of bioelectronic applications.

MATERIALS AND METHODS

Preparation of OECT channel materials

The channel material for the OECTs was composed of the PEDOT:PSS polymer (Clevios PH 1000, Heraeus), known for its high conductivity. The PH 1000 solution contained a solid material concentration ranging from 1 to 1.3%, with a weight ratio of PEDOT to PSS set at 1:2.5. To enhance the conductivity and reduce the surface tension of the PEDOT:PSS, a solution was formulated with 5% ethylene glycol and 0.1 wt % dodecyl benzene sulfonic acid. The solution was supplemented with 1 wt % of (3-glycidyloxypropyl) trimethoxysilane to enhance mechanical stability and promote adherence to the substrate. This formulated channel ink was filtered through a 0.45-μm polyethersulfone filter to eliminate unwanted particulates that could pattern uniformly.

Device fabrication

3D ES OECTs were fabricated on a flexible parylene-SR substrate using a silicon wafer as a base. Silicon wafers were deposited on a 2-μm parylene-SR using chemical vapor deposition (OBT-PC300, Obang Technology). The source and drain electrodes were fabricated from gold on the parylene substrate using standard photolithographic processes. Subsequent to the deposition of an additional 2-μm layer of parylene-SR, a second round of photolithography was conducted to expose the electrodes and contact pads using AZ GXR-601 photoresist (AZ Electronic Materials, Luxembourg). This was followed by spin coating the wafer at 1500 rpm for 60 s and a subsequent baking process at 110°C for 90 s. For defining the active channel area, the wafers were exposed by laser (250 mJ/cm^2) using photolithography (MLA-150, Heidelberg Instruments). The wafers were then developed in an AZ 300MIF (Merck) for 35 s. Next, the substrate was etched using reactive ion etching (RIE) [CIONE 6, Femto Science, Republic of Korea, 150 W/O_2 60 standard cubic centimeter per minute (sccm)] to expose the metal regions. Subsequently, the conducting polymer was patterned to form the active channel. The channels were baked at 130°C for 1 hour to produce a cross-linked PEDOT:PSS film and immersed into deionized water overnight to remove any residual compounds. To fabricate micro- and nanopatterns of the channel, a third lithography was conducted. For microstructured channels, the same photolithography method as described above was used. In contrast, for nanostructured channels, e-beam lithography was used. A positive e-beam resist (950 PMMA A2, MicroChem) was spin coated on the wafers that have cross-linked PEDOT:PSS channel of OECTs at 4000 rpm for 1 min. Next, baking on a hot plate at 180°C was applied for 5 min. The coated photoresist was exposed using e-beam lithography (ELS-7000, Elionix) at an acceleration voltage of 80 keV and beam current of 100 pA. The exposed resist was developed by immersing it in solution (MIBK/IPA 1:3). Next, the sample was etched using RIE (CIONE 6, Femto Science, Republic of Korea, 150 W/O_2 60 sccm) to produce a nanopattern channel. After etching, the remaining resist is removed by acetone.

The process of fabricating 3D ES OECT-based neural probes is completed by adding the interconnection section to the OECT fabrication process described earlier. It is noted that the interconnect lines were intentionally designed with a width of 200 μm to reduce undesired voltage losses across the interconnects. Anisotropic conductive film bonding was performed to connect the device to commercial external zero insertion force connectors using flexible flat cables (FFCs).

Device characterization

Electrical characterizations were conducted using a 0.01 M phosphate-buffered saline solution. The OECT gate electrode was coupled with an Ag/AgCl electrode and submerged in the electrolyte. Transfer characteristics and g_m-frequency characteristics were acquired by using a semiconductor device analyzer (Keysight B1500A and Keithley 4200A). All measurements were carried out under ambient conditions. Impedance spectroscopy was performed using a PalmSens4 impedance analyzer (PalmSens, Netherlands), applying a 30-mV sinusoidal potential at an offset bias of 0 V across a frequency range of 1 Hz to 1 MHz. Transient drain current responses were recorded using an ultrafast pulse measurement system (4225-PMU, Keithley). A stylus profiler (Bruker, Dektak XT) was used to measure the thickness of the PEDOT:PSS film. The measurements were executed at a speed of 0.1 mm s^{-1} with a stylus force of 3 mg. Nanoscale surface topology data were collected using tapping mode AFM (model: NanoScope V, Bruker and Jupiter XR, Oxford). Field-emission SEM and critical-dimension–SEM images were from models of JSM 7800F PRIME, JEOL Ltd., and 9380II Hitachi, respectively.

In vivo evaluation

All animal experiments were performed and handled in accordance with the regulations of the Institutional Animal Care and Use Committee of the Pukyong National University (approval no. 2023-046). For the ES OECT implantation, male Sprague-Dawley rats (300 g) were anesthetized with isoflurane. Initially, anesthesia was induced with 5% isoflurane in 100% oxygen (0.5 liters/min) for 5 min in an induction chamber. Once the pedal reflexes were lost, the hair was shaved. During the procedure, a nose cone provided continuous 2% isoflurane via a calibrated vaporizer. After achieving a deep level of anesthesia, the incision in the skin was expanded toward the dorsal region of the paw to reveal the musculature of the hind limb. Next, the muscles known as lateralis and biceps femoris were identified and subsequently retracted in order to expose the sciatic nerve. Subsequently, the OECT device was carefully wrapped around the sciatic nerve following the excision of the adjacent tissue. The ES OECT device was connected via an FFC, and a power supply was used to bias the transistors' drains. The recorded neural signals were amplified, band-pass filtered in the range of 300 Hz to 5 kHz, and digitized at a 30-kHz sampling rate using an RHD Recording headstage controller (RHD2132, Intan Technologies). For certain analyses, recordings underwent additional digital filtering with a 60-Hz notch filter and a band-pass filter to determine the SNR. SNR was computed using the peak of the highest activity and the root mean square noise during periods of minimal biological activity.

Supplementary Materials

This PDF file includes:

Figs. S1 to S8

Tables S1 and S2

REFERENCES AND NOTES

1. D. T. Simon, E. O. Gabrielsson, K. Tybrandt, M. Berggren, Organic bioelectronics: Bridging the signaling gap between biology and technology. *Chem. Rev.* **116**, 13009–13041 (2016).
2. M. Zhang, Z. Tang, X. Liu, J. Van der Spiegel, Electronic neural interfaces. *Nat. Electron.* **3**, 191–200 (2020).
3. S. Baek, Y. Lee, J. Baek, J. Kwon, S. Kim, S. Lee, K.-P. Strunk, S. Stehlin, C. Melzer, S.-M. Park, H. Ko, S. Jung, Spatiotemporal measurement of arterial pulse waves enabled by wearable active-matrix pressure sensor arrays. *ACS Nano* **16**, 368–377 (2022).
4. S. Baek, H. Matsui, T. Mano, J. A. Park, Y. Jo, Y. Lee, S. Tokito, J. Kwon, S. Jung, Dual-gate thin film transistor lactate sensors operating in the subthreshold regime. *Biosens. Bioelectron.* **222**, 114958 (2023).
5. L. Bai, C. G. Elósegui, W. Li, P. Yu, J. Fei, L. Mao, Biological applications of organic electrochemical transistors: Electrochemical biosensors and electrophysiology recording. *Front. Chem.* **7**, 313 (2019).
6. A. Marks, S. Griggs, N. Gasparini, M. Moser, Organic electrochemical transistors: An emerging technology for biosensing. *Adv. Mater. Interfaces* **9**, 2102039 (2022).
7. X. Ji, X. Lin, J. Rivnay, Organic electrochemical transistors as on-site signal amplifiers for electrochemical aptamer-based sensing. *Nat. Commun.* **14**, 1665 (2023).
8. S. Wang, X. Chen, C. Zhao, Y. Kong, B. Lin, Y. Wu, Z. Bi, Z. Xuan, T. Li, Y. Li, W. Zhang, E. Ma, Z. Wang, W. Ma, An organic electrochemical transistor for multi-modal sensing, memory and processing. *Nat. Electron.* **6**, 281–291 (2023).
9. S. T. M. Tan, A. Giovannitti, A. Melianas, M. Moser, B. L. Cotts, D. Singh, I. McCulloch, A. Salleo, High-gain chemically gated organic electrochemical transistor. *Adv. Funct. Mater.* **31**, 2010868 (2021).
10. Y. Lee, A. Carnicer-Lombarte, S. Han, B. J. Woodington, S. Chai, A. G. Polyravas, S. Velasco-Bosom, E. H. Kim, G. G. Malliaras, S. Jung, Tunable organic active neural probe enabling near-sensor signal processing. *Adv. Mater.* **35**, e2301782 (2023).
11. J. Chen, W. Huang, D. Zheng, Z. Xie, X. Zhuang, D. Zhao, Y. Chen, N. Su, H. Chen, R. M. Pankow, Z. Gao, J. Yu, X. Guo, Y. Cheng, J. Strzalka, X. Yu, T. J. Marks, A. Facchetti, Highly stretchable organic electrochemical transistors with strain-resistant performance. *Nat. Mater.* **21**, 564–571 (2022).
12. I. Uguz, D. Ohayon, S. Yilmaz, S. Griggs, R. Sheelamanthula, J. D. Fabbri, I. McCulloch, S. Inal, K. L. Shepard, Complementary integration of organic electrochemical transistors for front-end amplifier circuits of flexible neural implants. *Sci. Adv.* **10**, eadi9710 (2024).
13. S. Han, A. G. Polyravas, S. Wustoni, S. Inal, G. G. Malliaras, Integration of organic electrochemical transistors with implantable probes. *Adv. Mater. Technol.* **6**, 2100763 (2021).
14. M. Cucchi, C. Gruener, L. Petrauskas, P. Steiner, H. Tseng, A. Fischer, B. Penkovsky, C. Matthus, P. Birkholz, H. Kleemann, K. Leo, Reservoir computing with biocompatible organic electrochemical networks for brain-inspired biosignal classification. *Sci. Adv.* **7**, eabh0693 (2021).
15. X. Ji, B. D. Paulsen, G. K. Chik, R. Wu, Y. Yin, P. K. Chan, J. Rivnay, Mimicking associative learning using an ion-trapping non-volatile synaptic organic electrochemical transistor. *Nat. Commun.* **12**, 2480 (2021).
16. G. M. Matrone, E. R. van Doremaele, A. Surendran, Z. Laswick, S. Griggs, G. Ye, I. McCulloch, F. Santoro, J. Rivnay, Y. van de Burgt, A modular organic neuromorphic spiking circuit for retina-inspired sensory coding and neurotransmitter-mediated neural pathways. *Nat. Commun.* **15**, 2868 (2024).
17. S. Yamamoto, G. G. Malliaras, Controlling the neuromorphic behavior of organic electrochemical transistors by blending mixed and ion conductors. *ACS Appl. Electron. Mater.* **2**, 2224–2228 (2020).
18. C. Han, M. Kim, S. J. Park, J. S. Eo, D. Kim, Y. R. Park, S. Jung, G. Wang, Reconfigurable organic electrochemical transistors with high dynamic ranges for fully integrated physical reservoir computing. *Adv. Funct. Mater.* **35**, 2423814 (2025).
19. D. Khodagholy, J. Rivnay, M. Sessolo, M. Gurfinkel, P. Leleux, L. H. Jimison, E. Stavrinidou, T. Herve, S. Sanaur, R. M. Owens, G. G. Malliaras, High transconductance organic electrochemical transistors. *Nat. Commun.* **4**, 2133 (2013).
20. S. Chai, Y. Lee, R. M. Owens, H.-R. Lee, Y. Lee, W. Kim, S. Jung, Dynamic monitoring of a 3D-printed airway tissue model using an organic electrochemical transistor. *Biomaterials* **314**, 122806 (2025).
21. S. Wang, Y. Wang, X. Cai, B. Wang, C. Zhao, G. Pan, C. Harder, Y. Bulut, B. Zhang, S. Zhang, Y. Kong, K. Huang, B. Xie, P. Müller-Buschbaum, S. V. Roth, L. Yang, Y. Li, Y. Han, G. Bao, W. Ma, A high-frequency artificial nerve based on homogeneously integrated organic electrochemical transistors. *Nat. Electron.* **8**, 254–266 (2025).
22. M. Zijlmans, G. A. Worrell, M. Dümpelmann, T. Stieglitz, A. Barborica, M. Heers, A. Ikeda, N. Usui, M. Le Van Quyen, How to record high-frequency oscillations in epilepsy: A practical guideline. *Epilepsia* **58**, 1305–1315 (2017).
23. M. Sharifshazileh, K. Burelo, J. Sarnthein, G. Indiveri, An electronic neuromorphic system for real-time detection of high frequency oscillations (HFO) in intracranial EEG. *Nat. Commun.* **12**, 3095 (2021).
24. Z. M. Nikolic, D. B. Popovic, R. B. Stein, Z. Kenwell, Instrumentation for ENG and EMG recordings in FES systems. *IEEE Trans. Biomed. Eng.* **41**, 703–706 (1994).
25. A. Diedrich, W. Charoensuk, R. J. Brychta, A. C. Ertl, R. Shiavi, Analysis of raw microneurographic recordings based on wavelet de-noising technique and classification algorithm: Wavelet analysis in microneurography. *IEEE Trans. Biomed. Eng.* **50**, 41–50 (2003).
26. N. V. Thakor, *Handbook of Neuroengineering* (Springer Nature, 2023).
27. G. Buzsáki, C. A. Anastassiou, C. Koch, The origin of extracellular fields and currents—EEG, ECoG, LFP and spikes. *Nat. Rev. Neurosci.* **13**, 407–420 (2012).
28. Y. Lee, J. Kwon, S. Jung, W. Kim, S. Baek, S. Jung, Reliable inkjet contact metallization on printed polymer semiconductors for fabricating staggered TFTs. *Appl. Phys. Lett.* **116**, 153301 (2020).
29. W. Kim, G. Ryu, Y. Nam, H. Choi, M. Wang, J. Kwon, C. B. Nielsen, K. Kang, S. Jung, High mobility amorphous polymer-based 3D stacked pseudo logic circuits through precision printing. *Adv. Funct. Mater.* **34**, 2312922 (2024).
30. J. Kwon, Y. Takeda, R. Shiwaku, S. Tokito, K. Cho, S. Jung, Three-dimensional monolithic integration in flexible printed organic transistors. *Nat. Commun.* **10**, 54 (2019).
31. J. Rivnay, S. Inal, A. Salleo, R. M. Owens, M. Berggren, G. G. Malliaras, Organic electrochemical transistors. *Nat. Rev. Mater.* **3**, 17086 (2018).
32. C. M. Proctor, J. Rivnay, G. G. Malliaras, Understanding volumetric capacitance in conducting polymers. *J. Polym. Sci. B Polym. Phys.* **54**, 1433–1436 (2016).
33. J. Rivnay, P. Leleux, M. Ferro, M. Sessolo, A. Williamson, D. A. Koutsouras, D. Khodagholy, M. Ramuz, X. Strakosas, R. M. Owens, C. Benar, J. M. Badier, C. Bernard, G. G. Malliaras, High-performance transistors for bioelectronics through tuning of channel thickness. *Sci. Adv.* **1**, e1400251 (2015).
34. P. Leleux, J. Rivnay, T. Lonjaret, J. M. Badier, C. Bénar, T. Hervé, P. Chauvel, G. G. Malliaras, Organic electrochemical transistors for clinical applications. *Adv. Healthc. Mater.* **4**, 142–147 (2015).
35. M. Stephen, X. Wu, T. Li, T. Salim, K. Hou, S. Chen, W. L. Leong, Crown ether enabled enhancement of ionic–electronic properties of PEDOT:PSS. *Mater. Horiz.* **9**, 2408–2415 (2022).
36. J. T. Friedlein, M. J. Donahue, S. E. Shaheen, G. G. Malliaras, R. R. McLeod, Microsecond response in organic electrochemical transistors: Exceeding the ionic speed limit. *Adv. Mater.* **28**, 8398–8404 (2016).
37. M. J. Donahue, A. Williamson, X. Strakosas, J. T. Friedlein, R. R. McLeod, H. Gleskova, G. G. Malliaras, High-performance vertical organic electrochemical transistors. *Adv. Mater.* **30**, 1705031 (2018).
38. W. Huang, J. Chen, Y. Yao, D. Zheng, X. Ji, L.-W. Feng, D. Moore, N. R. Glavin, M. Xie, Y. Chen, R. M. Pankow, A. Surendran, Z. Wang, Y. Xia, L. Bai, J. Rivnay, J. Ping, X. Guo, Y. Cheng, T. J. Marks, A. Facchetti, Vertical organic electrochemical transistors for complementary circuits. *Nature* **613**, 496–502 (2023).
39. J. Brodský, I. Gablech, L. Migliaccio, M. Havlíček, M. J. Donahue, E. D. Głowacki, Downsizing the channel length of vertical organic electrochemical transistors. *ACS Appl. Mater. Interfaces* **15**, 27002–27009 (2023).
40. M. Skowrons, A. Schander, A. G. P. Negron, B. Lüssem, The trade-off between transconductance and speed for vertical organic electrochemical transistors. *Adv. Electron. Mater.* **10**, 2300673 (2024).
41. J. Wang, S. Lee, T. Yokota, Y. Jimbo, Y. Wang, M. O. G. Nayeem, M. Nishinaka, T. Someya, Nanomesh organic electrochemical transistor for comfortable on-skin electrodes with local amplifying function. *ACS Appl. Electron. Mater.* **2**, 3601–3609 (2020).
42. J. Wang, S. Lee, T. Yokota, T. Someya, Gas-permeable organic electrochemical transistor embedded with a porous solid-state polymer electrolyte as an on-skin active electrode for electrophysiological signal acquisition. *Adv. Funct. Mater.* **32**, 2200458 (2022).
43. S. K. Lee, Y. W. Cho, J. S. Lee, Y. R. Jung, S. H. Oh, J. Y. Sun, S. Kim, Y. C. Joo, Nanofiber channel organic electrochemical transistors for low-power neuromorphic computing and wide-bandwidth sensing platforms. *Adv. Sci.* **8**, 2001544 (2021).
44. S.-H. Oh, M. Oh, S. Lee, D.-K. Kim, J.-S. Lee, S.-K. Lee, S.-K. Kang, Y.-C. Joo, Fast and durable nanofiber mat channel organic electrochemical transistors. *ACS Appl. Mater. Interfaces* **15**, 39614–39624 (2023).
45. G. D. Spyropoulos, J. N. Gelinas, D. Khodagholy, Internal ion-gated organic electrochemical transistor: A building block for integrated bioelectronics. *Sci. Adv.* **5**, eaau7378 (2019).
46. C. Cea, G. D. Spyropoulos, P. Jastrzebska-Perfect, J. J. Ferrero, J. N. Gelinas, D. Khodagholy, Enhancement-mode ion-based transistor as a comprehensive interface and real-time processing unit for in vivo electrophysiology. *Nat. Mater.* **19**, 679–686 (2020).
47. S. Y. Yeung, A. Veronica, Y. Li, I. M. Hsing, High-performance internal ion-gated organic electrochemical transistors for high-frequency bioimpedance analysis. *Adv. Mater. Technol.* **8**, 2201116 (2023).
48. S. Inal, G. G. Malliaras, J. Rivnay, Benchmarking organic mixed conductors for transistors. *Nat. Commun.* **8**, 1767 (2017).
49. P. R. Paudel, V. Kaphle, D. Dahal, R. K. Radha Krishnan, B. Lüssem, Tuning the transconductance of organic electrochemical transistors. *Adv. Funct. Mater.* **31**, 2004939 (2021).
50. P. Romele, M. Ghittorelli, Z. M. Kovács-Vajna, F. Torricelli, Ion buffering and interface charge enable high performance electronics with organic electrochemical transistors. *Nat. Commun.* **10**, 3044 (2019).

51. W. Lee, D. Kim, N. Matsuhisa, M. Nagase, M. Sekino, G. G. Malliaras, T. Yokota, T. Someya, Transparent, conformable, active multielectrode array using organic electrochemical transistors. *Proc. Natl. Acad. Sci. U.S.A.* **114**, 10554–10559 (2017).
52. I. Del Agua, L. Porcarelli, V. Curto, A. Sanchez-Sanchez, E. Ismailova, G. Malliaras, D. Mecerreyes, A Na+ conducting hydrogel for protection of organic electrochemical transistors. *J. Mater. Chem. B* **6**, 2901–2906 (2018).
53. E. Zeglio, M. Vagin, C. Musumeci, F. N. Ajjan, R. Gabrielsson, X. T. Trinh, N. T. Son, A. Maziz, N. Solin, O. Inganas, Conjugated polyelectrolyte blends for electrochromic and electrochemical transistor devices. *Chem. Mater.* **27**, 6385–6393 (2015).
54. P. Gkoupidenis, Y. Zhang, H. Kleemann, H. Ling, F. Santoro, S. Fabiano, A. Salleo, Y. van de Burgt, Organic mixed conductors for bioinspired electronics. *Nat. Rev. Mater.* **9**, 134–149 (2024).
55. B. D. Paulsen, K. Tybrandt, E. Stavrinidou, J. Rivnay, Organic mixed ionic–electronic conductors. *Nat. Mater.* **19**, 13–26 (2020).
56. J. Tropp, D. Meli, J. Rivnay, Organic mixed conductors for electrochemical transistors. *Matter* **6**, 3132–3164 (2023).
57. R. Wu, X. Ji, Q. Ma, B. D. Paulsen, J. Tropp, J. Rivnay, Direct quantification of ion composition and mobility in organic mixed ionic-electronic conductors. *Sci. Adv.* **10**, eadn8628 (2024).

Acknowledgments

Funding: This research was supported by the National Research Foundation of Korea (NRF) grants funded by the Korea government (MSIT) (NRF-2022R1A2C2012272 and RS-2024-00403376 to S.J.) and by the Basic Science Research Program through the NRF funded by the Ministry of Education (RS-2024-00337597 to K.-I.S.). **Author contributions:** Conceptualization: Y.L., J.K., and S.J. Experiments: Y.L. and S.J.P. Data analysis: Y.L., S.J.P., and J.K. Visualization: Y.L. and S.J.P. Animal experiment design and supervision: K.-I.S. Supervision: S.J. Project administration: S.J. Funding acquisition: S.J. and K.-I.S. Writing—original draft: Y.L., S.J.P., and S.J. Writing—review and editing: Y.L., S.J.P., K.-I.S., J.K., and S.J. **Competing interests:** The authors declare that they have no other competing interests. S.J. and Y.L. declare that a patent application related to the technology described in this work has been filed (patent application no. KR10-2024-0008574; filed on 19 January 2024; applicant, POSTECH Research and Business Development Foundation). **Data and materials availability:** All data needed to evaluate the conclusions in the paper are present in the paper and/or the Supplementary Materials.

Submitted 7 April 2025
Accepted 25 August 2025
Published 26 September 2025
10.1126/sciadv.ady0279

ScienceAdvances

Addressing transconductance-bandwidth trade-off by three-dimensional electrolyte-surrounded organic electrochemical transistors

Yongwoo Lee, Seong Jun Park, Jimin Kwon, Kang-Il Song, and Sungjune Jung

Sci. Adv. **11** (39), eady0279. DOI: 10.1126/sciadv.ady0279

Science Advances (ISSN 2375-2548) is published by the American Association for the Advancement of Science. 1200 New York Avenue NW, Washington, DC 20005. The title *Science Advances* is a registered trademark of AAAS.